Journal of Materials Chemistry C

Colloidal Quantum Dot Based Infrared Detectors: Extending to the Mid-Infrared and Moving from the Lab to the Field

Journal:	*Journal of Materials Chemistry C*
Manuscript ID	TC-REV-11-2021-005359.R1
Article Type:	Review Article
Date Submitted by the Author:	04-Dec-2021
Complete List of Authors:	Nakotte, Tom; Lawrence Livermore National Laboratory, Munyan, Simon; University of California Santa Barbara Murphy, John; Lawrence Livermore National Laboratory Hawks, Steven; Lawrence Livermore National Laboratory, PLS MSD Kang, ShinYoung; Lawrence Livermore National Laboratory Han, Jinkyu; SUNY Stony Brook, Hiszpanski, Anna; Lawrence Livermore National Laboratory, Materials Science Division

ARTICLE

Received 00th January 20xx,
Accepted 00th January 20xx

DOI: 10.1039/x0xx00000x

Colloidal Quantum Dot Based Infrared Detectors: Extending to the Mid-Infrared and Moving from the Lab to the Field

Tom Nakotte[a,*], Simon G. Munyan[a,b,*], John W. Murphy[c], Steven A. Hawks[a], ShinYoung Kang[a], Jinkyu Han[a], Anna M. Hiszpanski[a,†]

Quantum dots (QDs) that absorb in the mid-wave infrared (MWIR) regime (3-5 μm) have recently generated significant interest as possible detector materials for MWIR cameras, with promises to reduce materials and device fabrication costs and potentially increase device operating temperatures. However, these materials have been primarily explored in single pixel devices – not multi-pixel cameras – and their current performance lags behind that of commercially available MWIR cameras based on single crystalline materials. To realize the potential of QD MWIR photodetectors with imaging capabilities, improvements are needed in the quality of the MWIR-absorbing QD materials, ligands dictating inter-QD charge transport, ordering of QD films, device architectures, and scalability of these methods to larger areas. With three families of QDs being researched -- lead-, silver-, and mercury-based chalcogenides -- as well as a multitude of possible capping ligands and film deposition techniques, the experimental phase space for MWIR QDs is vast. In this review, we provide a roadmap, considering the pros and cons of various film deposition and ligand exchange techniques, as well as reintroduce lessons learned over years of research on QD film formation. We also extracted and created a database of reported quantum dot photodetectors' performance and fabrication methods and have developed an interactive data visualization dashboard for this database, which provides researchers in the field a quick snapshot of the existing state of the art. Finally, we outline figures of merit and information that should be presented in papers moving forward which would help to clarify the reported results, as well as offer ideas for future steps. We provide a database visualization of the QD photodetector literature at https://public.tableau.com/app/profile/tom.nakotte/viz/IRQDphotodetectors_16384709473480/Dashboard1#1.

Introduction

In the 3-5 μm regime, commonly referred to as the mid-wave infrared (MWIR), chemical bonds absorb light, enabling chemical identification using MWIR detectors for chemical manufacturing and astronomy. Additionally, hot objects, such as living beings or machinery in operation, emit infrared radiation in the MWIR that scales with the temperature of the object, enabling thermal imaging that is used for defense, security, and tracking applications. However, despite their broad potential applicability, MWIR photodetectors are not as ubiquitously utilized as their visible counterparts and lag behind in terms of their collective image quality, cost, size, and weight characteristics. Specifically, MWIR detectors have a trade-off between performance and cost depending on the principle of their operation, which is either thermal or photonic/quantum. Thermal MWIR detectors, like bolometers, thermocouples, and pyroelectrics, produce a change in resistance or voltage based on a change in the detector temperature upon absorbing incident radiation. Such detectors do not have to be cooled (reducing size and weight) and are low-cost, making them common in consumer IR imaging devices; however, these cameras suffer from poor performance compared to their photonic/quantum counterparts (*i.e.*, slower response and lower detectivity). In photonic, or quantum, detectors absorption of incident radiation excites electrons into non-equilibrium states, which produces a detectable electrical

[a] *Materials Science Division, Lawrence Livermore National Laboratory, 7000 East Ave, Livermore, CA 94550.*
[b] *Materials Research Laboratory, University of California, Santa Barbara, CA 93106*
[c] *Materials Engineering Division, Lawrence Livermore National Laboratory, 7000 East Ave, Livermore, CA 94550*
**Co-first authors*
† Corresponding author
Electronic Supplementary Information (ESI) available: [details of any supplementary information available should be included here]. See DOI: 10.1039/x0xx00000x

current. Photonic detectors are generally higher speed and provide excellent detectivity when cooled to cryogenic temperatures but require expensive materials (e.g., single crystalline HgCdTe or InSb wafers grown by molecular beam epitaxy (MBE)), and the cooling requirement further increases the cost and physical footprint of imaging systems. An ongoing challenge is to create detectors that can operate at higher temperatures without sacrificing performance and while simultaneously yielding lower cost, size, weight, and power requirements. Solving this challenge would enable fully realizing and expanding the potential of MWIR detectors across their broad potential applicability space.

Quantum dot (QD) based photonic MWIR cameras are a promising alternative to current MWIR detector technologies, with the potential to combine the low cost of thermal detectors and higher detectivity of current photonic detectors. QDs are semiconductor particles with nanoscale dimensions that display altered optical and electronic properties, such as quantized energy levels and long exciton lifetimes, when compared to their bulk counterparts due to the quantum confinement effect.[1] These altered properties can be beneficial for optoelectronic devices. For example, the quantization of energy levels provides tunable absorption that is controlled by the QDs' particle size.[2] Likewise, the longer exciton lifetimes exhibited by QDs increases the likelihood of photogenerated carriers being collected by an electrode before recombining, which results in higher internal quantum efficiencies in detectors.[3] While QDs can be produced either via molecular beam epitaxy[4,5] or in solution yielding colloidal QDs,[6] commercialization of epitaxially-grown QD MWIR cameras seems unlikely. Epitaxially grown QDs are significantly more costly to produce, are less densely packed, and are not solution processable, which makes device fabrication more challenging. Colloidal synthesis methods are the most robust method of fabricating quantum dots when factoring cost,[7] size control,[2,8,9] and flexibility for film deposition.[10–14] Thus, this review will focus exclusively on devices fabricated from colloidal QDs.

Much of the early research in colloidal QD-based optoelectronic devices centered around solar cells[15] and light emitting diodes (LEDs) in the visible wavelength regime,[16] but recently research on colloidal QDs has moved to longer wavelengths, extending across the infrared regime (from short-wave (1-3 μm) (SWIR) to long-wave (8-12 μm)), for IR photodetectors and cameras. Currently, extending the operation of quantum dot-based devices into the mid-wave infrared (and beyond) is the frontier of quantum dot optoelectronic research, and thus this review focuses particularly on materials and devices suited for this wavelength regime. However, it is informative to capture the techniques and performance of prior quantum dot-based optoelectronic devices that were aimed at shorter wavelengths, notably the SWIR and visible regimes. While more recent QD work is focused on longer wavelength regimes and application areas than earlier work on colloidal QDs, many of the lessons learned from those earlier studies are applicable to this new wavelength regime and application space. The solution-processability of colloidal QDs enables their easier integration with complimentary-metal-oxide-semiconductor (CMOS) architectures and read-out integrated circuits (ROICs) compared to current technology, which requires indium bump

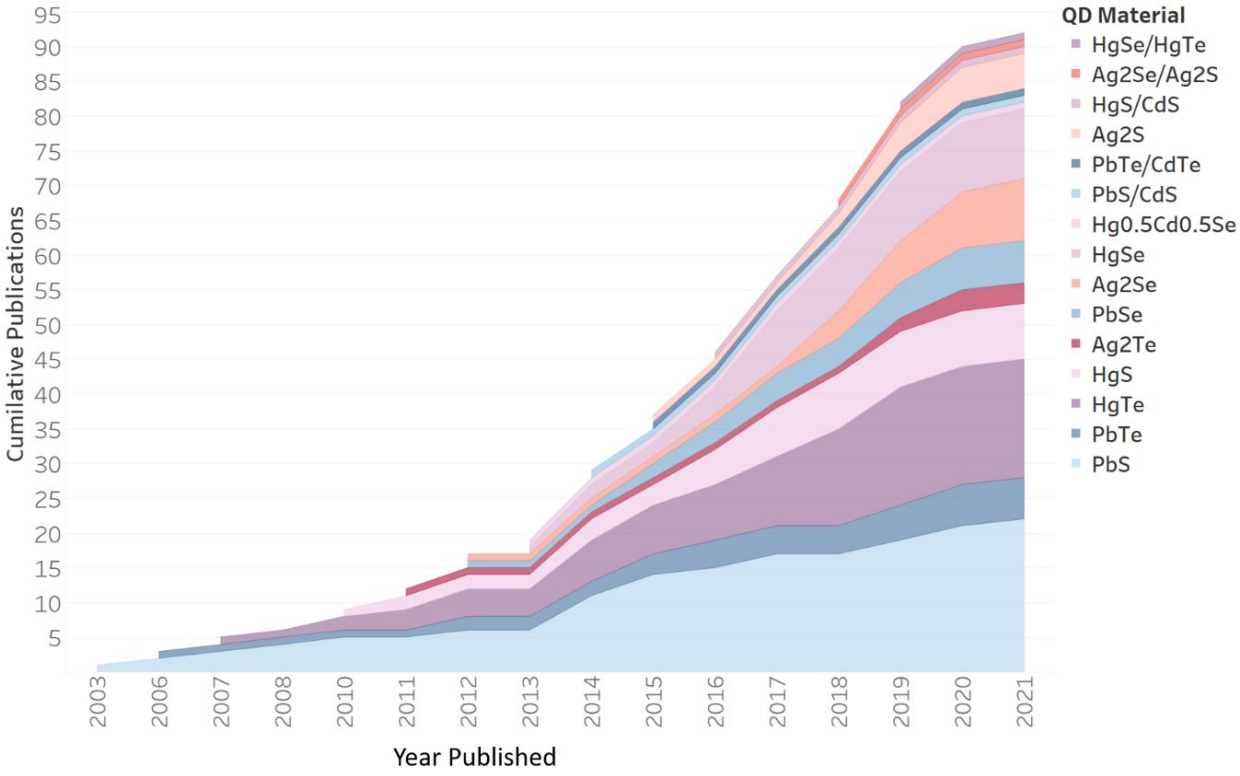

Figure 1: Running sum of published articles from 2003 to Oct2021 pertaining to SWIR and MWIR QD detectors with colors representing the specific QD material system investigated.

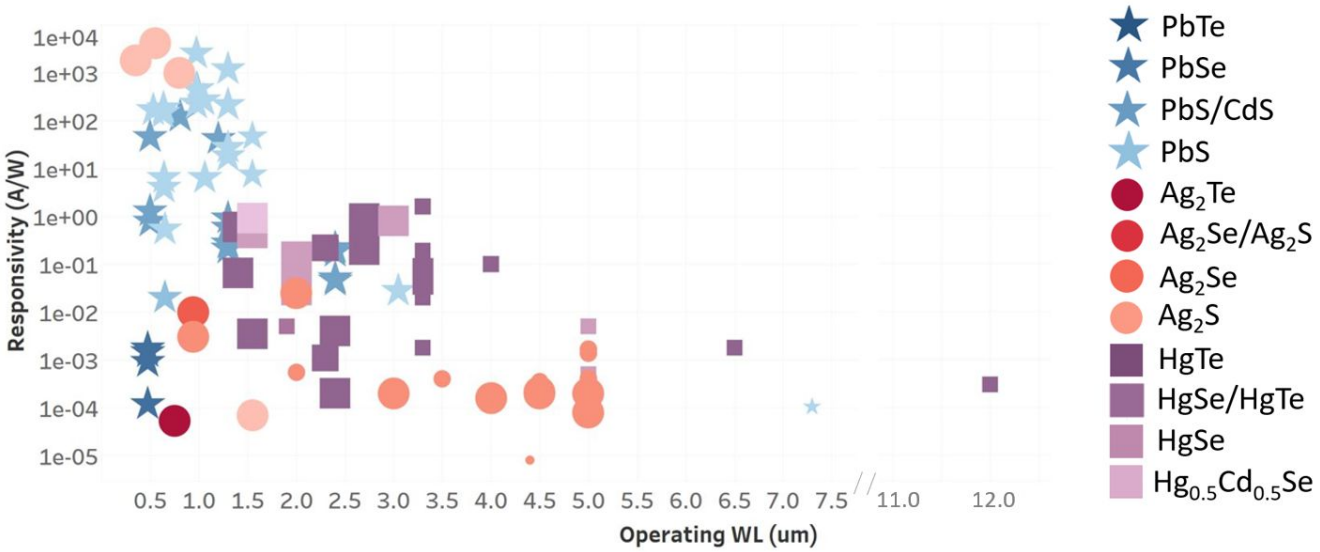

Figure 2: Responsivity as a function of wavelength and QD material. Size of marker is indicative of measurement temperature with largest markers having a measurement temperature of 300K and smallest markers 25K, note the break in the x-axis from 7.5 to 11 µm. Shape and color correspond to different QD material

bonding to mate the rigid single-crystalline detector material with the rigid CMOS or ROIC substrates. A simple production cost analysis showed that QDs can be produced for $10-$60 per gram,[7] making materials costs much lower than the current means of creating IR detectors from single crystal wafers and MBE-grown quantum wells.[17]

In this review, we provide an overview of the progress in IR-sensitive QD materials' development, surface chemistries, deposition techniques, and single-pixel photodetector device architectures. We take a comprehensive and quantitative approach to assess the state of the QD IR photodetector field by extracting details on materials' chemistries and single-pixel device's construction from all articles pertaining to QD IR photodetectors, creating the first database for the QD IR field. We provide a visualization of this database for others to utilize and build upon; it is freely available at https://public.tableau.com/app/profile/tom.nakotte/viz/IRQDphotodetectors_16384709473480/Dashboard1#1, and the visualizations and insights from them are discussed throughout the review. We highlight areas where further developments are required and the potential means of achieving them to enhance the performance of QD-based IR photodetectors for potential commercialization. Of particular importance for commercialization, few demonstrations have been made of multi-pixel QD IR cameras. In the last section of the review, we discuss the few examples made thus far, what challenges must still be addressed in scaling from single- to multi-pixel devices and provide guidance on best practices.

Overview of the QD IR Detector Field

Figure 1 shows the running sum of published articles that we collected pertaining to QD-based SWIR and MWIR detectors, showing how interest has grown in this field since the earliest reports in 2003. This figure is included in our database visualization, and a complete list of the articles we collected and analyzed throughout this article is provided in the SI. In **Figure 1**, the color pertains to the QD materials system, also showing the diversity of materials explored for this application space, and how interest in some particular materials systems increased in recent years. Generally, the three most common families of QDs used in the fabrication of MWIR sensitive detectors are: lead chalcogenides, mercury chalcogenides, and silver chalcogenides. Lead chalcogenides are the most well-established family of the three with the first report of PbS (light blue in **Figure 1**) QD photodetectors in 2003; however, many of these early reports focus on SWIR regime rather than the MWIR. Currently, the Pb-based quantum dots lead the field in number of publications, while Hg-based quantum dots follow closely behind.[18] Ag-based quantum dots have received far fewer publications and are the "new kids on the block", but the exclusion of toxic heavy metals makes this family appealing from health and environmental safety perspectives.

Responsivity (R) is one primary figures of merit reported in the literature for IR photodetectors, and in **Figure 2** – another subfigure of our database visualization – we show all responsivities of QD-based single-pixel photodetectors reported since 2003 as a function of their operating wavelength. The responsivity specifically characterizes the amount of signal current collected per Watt of incident light where a higher responsivity indicates a more sensitive or efficient device. In Figure 2, the symbol and color of each datapoint indicates the QD materials system and the size of the datapoint represents the temperature at which the device was operating, with the largest symbol indicative of room temperature. The device's operating temperature has a significant effect on performance metrics because cooling the device decreases hot carriers and results in lower dark current. Two trends are immediately apparent from Figure 2. The first is how the number of photodetector demonstrations drops off with increasing operational wavelengths. Many more photodetector devices have been demonstrated below 3 µm in the visible, near-IR and

SWIR regime than in the 3-5 µm MWIR regime, and the LWIR regime is even more sparsely populated, with only one report beyond 8 µm.[19] The second is how the reported responsivities decrease with increasing operational wavelengths. One fundamental reason for the decrease in responsivity at longer wavelengths is the background limited infrared photodetector limit,[20] which is a result of generation-recombination noise due to background blackbody radiation.[21] However, other factors including material/synthesis limitations and thermal effects causing higher dark currents can also impact the responsivity at longer wavelengths. In the MWIR regime of interest in this review, mercury chalcogenides have produced the highest responsivities to date and are the most versatile material in that they can achieve MWIR sensitivity through interband and intraband transitions, a distinction that will be discussed in greater detail in the synthesis portion of this review.

Synthesis

Many variables during colloidal QD synthesis can affect the quality and properties of QDs, including the ligand type,[22,23] air exposure,[24] metal precursor, chalcogen precursor,[25] and purification technique.[26] As with any system, the performance of the final product, in this case the photodetector, is significantly impacted by the quality of the building blocks, the QDs. Therefore, we first briefly review the advancements made in colloidal synthesis and present some challenges that remain to be solved. Note this is only a short overview and a more in-depth discussion of colloidal synthesis advancements can be found elsewhere.[18,27–29]

The most well-researched family of QDs with potential for MWIR detection are the lead chalcogenides, with significant strides in size/shape control,[30] air stability,[31] and shelling techniques.[32] However, much of this research has been done primarily on QDs absorbing in SWIR rather than MWIR. Pb-based QD devices use interband transitions as a source of created photocarriers, which results in the excitation of electrons from the $1S_h$ valence band state to the $1S_e$ conduction band state, as shown in **Figure 3A**. Devices utilizing interband transitions are limited in their wavelength sensitivity range by the bulk bandgap of the material, which is 0.26 eV (≈4.7 µm) and 0.41 eV (≈3 µm) for PbSe and PbS, respectively. From this bulk bandgap value, the QDs' bandgap can only increase, thereby shifting absorption to smaller wavelengths, as the QD size becomes smaller and quantum confinement is enhanced. Therefore, materials with a bulk bandgap in the MWIR range are challenging to create MWIR-absorbing QDs from because doing so would require fairly large QDs,[33] and as QD size increases, additional challenges arise due to poor air stability and low quantum efficiency. For example, large PbSe QDs (>16 nm) with interband transitions of ~4 µm reaching the MWIR have been reported, but they remain intractable for MWIR photodetectors due to poor quantum yield and air stability.[2] The most common method to improve air stability as well as quantum yield in lead chalcogenide QDs is using cation exchange to grow a cadmium chalcogenide shell around the lead chalcogenide core. However, lead chalcogenide QDs transition from spherical to cubic in shape as the diameter approaches 12nm,[2] and the cubic shape of large Pb-based QDs makes cation exchange difficult due to its faceted growth mechanism.[34]

An alternative approach to achieving MWIR sensitivity is through intraband transitions, which occur in doped systems via promotion of an electron from the $1S_e$ conduction band state to the $1P_e$ state, as depicted in **Figure 3B**. Recent research on heavily n-doped PbS QDs show that an intraband absorption

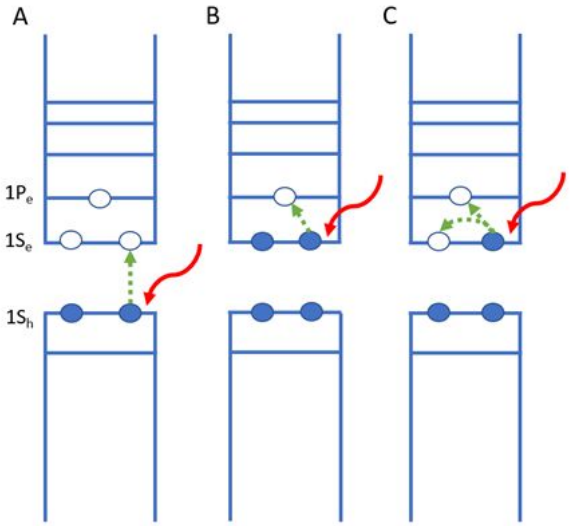

Figure 3: Schematic of energy states in a QD. (A) Interband transition in which an electron (filled circle) is promoted to the conduction band via absorption of a photon (red arrow). (B) Intraband absorption in an ideally doped QD. (C) Intraband absorption in a nonideally doped QD, where an electron is excited by photon; however, the presence of a hole state (unfilled circle) in the $1S_e$ state creates the possibility of recombination before promotion into the $1P_e$ state

peak at roughly 6-8 µm (depending on QD size) can be obtained, but this approach requires encapsulation via atomic layer deposition (ALD) after ligand exchange to prevent oxidation and loss of the intraband MWIR absorption.[35] While lead chalcogenide QDs may not be the most well-suited for MWIR applications, the extensive research on surface chemistries and synthetic conditions can provide valuable insight for possible routes of improvement in the mercury and silver chalcogenide material systems. For instance, ligand type has been shown to affect the Fermi level,[36] band edge positions,[22,37] and carrier type[38,39] in lead and mercury chalcogenide QD films, suggesting similar possibilities in silver-based QD films.

The challenges for lead chalcogenide QDs in the MWIR have led researchers to broaden the scope of materials to include mercury and silver chalcogenides. Mercury chalcogenides have extremely narrow or even negative (i.e., metallic) bandgaps in their bulk form at room temperature; however, quantum confinement allows these band gaps to be tuned into the MWIR and SWIR.[27] Most of the research in QD-based MWIR detectors in which interband transitions are the primary means of carrier generation has been with HgTe QDs, which have been reported to be photoconductive at the 5 µm upper MWIR limit.[40] Initially, synthesis of mercury chalcogenide QDs lagged behind other QD materials due to the toxicity and lack of availability of suitable

mercury precursors. However, as the QD community improved synthetic approaches to move away from the use of highly toxic mercury alkyls towards mercury-containing metal oxides and metal halides as precursors, mercury chalcogenide QDs began to be more widely reported.[27] Due to their propensity for self-doping from excess mercury that was discussed earlier, mercury chalcogenides can also achieve MWIR sensitivity through intraband transitions. The extent of QDs' doping is a critical variable affecting the performance of QD photodetectors that are based on MWIR absorption from intraband transitions. Ideally, the QDs' $1S_e$ state should be completely occupied to reduce the number of available holes that excited electrons can recombine with before being promoted to the $1P_e$ state. However, in practice, incomplete doping, such as what is depicted in **Figure 3C,** is commonly encountered. In a nonideally doped system, the $1S_e$ state is not entirely occupied, thereby increasing the likelihood of recombination with an available hole before the intraband transition to the $1P_e$ state. Such recombination reduces the quantum efficiency of the photodetector, thereby also reducing its responsivity. QD films with a fully doped $1S_e$ state will also show the strongest optical absorption and lowest dark conductivity, which in turn increases the responsivity of the devices.[40,41] Hg-based QDs have also been a leader for MWIR detectors utilizing intraband transitions due to their predisposition to self-doping.[42] The effect of capping ligand on intraband transitions in QDs is less well studied and quantified than their effect on the interband transitions, with only a few reports indicating that ligand choice has a significant effect on the strength of optical absorbance in the MWIR.[43–45]

With a growing desire to move away from materials containing toxic heavy metals like mercury and lead, silver chalcogenides have recently gained interest for applications in the MWIR. Ag_2Se is a promising candidate for QDs targeting the MWIR because its bulk bandgap is reported to be 0.05-0.18 eV, which corresponds to an absorption onset ranging from 24.8 to 6.9 µm.[46] Thus, in theory, one may expect that, with quantum confinement, Ag_2Se's bandgap can be tuned to correspond to MWIR wavelengths. However, in practice, the inter-bandgap absorbance of all Ag_2Se QDs has thus far corresponded to the near-IR (1080-1330 nm) (NIR), which may be due to the bulk bandgap of Ag_2Se being larger than what has been reported or may be due to the changes in crystal structure of Ag_2Se under quantum confinement (and therefore changes in the referenced bulk bandgap).[47] Though tuning the inter-bandgap absorption of Ag_2Se does not yield MWIR absorbance, silver chalcogenides also have the propensity to self-dope with an excess of Ag, resulting in the appearance of intra-bandgap transitions with strong MWIR absorbance.[48,49] The surface chemistry of silver chalcogenide QDs is the least well explored of the QD families presented in this review, but ligand choice has been shown to greatly affect intra-bandgap absorption in MWIR and carrier mobility.[44]

The library of capping ligands used in MWIR QD photodetectors is an area that has not received as much attention as it has for other application areas, such as QD solar cells. When selecting ligands for QD films, multiple factors must be taken into account, the most obvious of which is ligand length since long ligands hinder inter-QD charge transport.[50] However, the doping effect of the ligand on the QD film is a less studied factor that is of high importance in QD devices using intraband transitions. For example, 1,2-ethanedithiol (EDT) is one of the most commonly utilized ligands given its short length and ability to crosslink QDs, which typically leads to higher carrier mobilities in films; however, EDT can cause a condition of under-doping in Ag_2Se QD films, which results in partially filled bands and the introduction of trap states.[51] A systematic ligand study on Ag_2Se QD films shows that improved carrier mobility is not the only factor to consider when selecting a ligand, as increased optical absorption and control of carrier recombination greatly affect device performance.[44] Very few studies report on ligand choice in the mercury and silver chalcogenide families,[45,52,53] a variable that has been shown to affect carrier concentration in QD solar cells.[54,55] The best results in carrier mobility for mercury chalcogenides, with electron mobilities up to 100 cm^2/Vs, have been reported with the use of As_2S_3 as the capping ligand.[56] Thorough studies of capping ligand effects on optical and electronic properties of mercury and silver chalcogenide QDs are necessary to identify optimal ligand candidates for MWIR QD detectors, as current reports primarily utilize ligands that have been shown to be effective for other QD materials.

Ligand Exchange

Despite the differences in materials and surface chemistries between different QDs, some rules for creating QD films hold true universally. Initially, optoelectronic devices constructed from QD films suffered from poor carrier mobilities due to the long organic ligands used in synthesis to stabilize QDs in solution. Long ligands inhibit carrier transport because they are insulating and add physical distance between QDs within the film, resulting in a barrier for carrier hopping, which has been shown to be the predominant method of transport in QD films.[50] Decreasing the inter-QD spacing within films is traditionally accomplished via solid-state ligand exchange (also referred to as layer-by-layer or post-deposition ligand exchange) where long chain ligands are replaced by shorter ligands. In this process, a QD film is deposited onto a substrate, typically by drop-casting or spin-coating, and then subsequently exposed to a solution of shorter ligands (*e.g.,* EDT in ethanol) that replace the native ligands and allow the QDs to come into closer contact. Solid-state ligand exchange is typically performed on sufficiently thin QD films to allow for complete solution penetration and can result in film discontinuities due to the loss of volume previously taken up by longer ligands. The shortcomings of solid-state or layer-by-layer ligand exchange are particularly cumbersome when fabricating films thicker than 100nm due to the need to perform ligand exchange after each deposited layer to ensure compete ligand exchange throughout the film.

More recently, in-solution ligand exchange has been used to successfully prepare QD solutions[57–59] that can be made into charge-transporting thin films directly without the need for an

additional post-deposition ligand exchange step. In-solution ligand exchange techniques

are especially valuable for applications that require thicker (>100nm) QD films, as is generally desired for MWIR photodetectors, because they reduce the number of steps required to deposit a thick film and eliminate the possibility of deformations or cracks forming within the film due to laborious layer-by-layer ligand exchange. However, there are still significant challenges to be overcome for in-solution ligand exchange to become the predominant method of QD ligand exchange, which could improve ease of integration for commercial applications. Primarily, colloidal stability of QD solutions suffers after ligand exchange due to the shorter surface ligands' inability to prevent aggregation, resulting in eventual precipitation of particles. There has been one report of in-solution ligand exchanged QDs remaining colloidally stable for months; however this technique uses an uncommon solvent (2,6-diflouropyridine) and has only been demonstrated on lead chalcogenide QDs.[23] Another paper reports QDs prepared with short thioglycerol ligands that can be dispersed in water, but in order to prevent the QDs' conglomeration, the solution concentration must be low, which makes uniform film formation difficult.[60]

Regardless of whether solid state or in-solution ligand exchange is used to prepare a QD film, deposition is typically followed by a thermal annealing step to promote sintering of QD facets and further improve carrier transport.[50,61,62] An annealing step typically consists of heating the substrate between 90-120 deg C for minutes to an hour in an inert atmosphere.[61] While sintering of the QDs improves carrier mobility within the film, over-annealing can result in a loss of quantum confinement, which will adversely affect the lifetime of photogenerated carriers and the film's absorption edge, resulting in higher dark currents.[63]

To see if any trends exist in how choice of ligand or ligand exchange method may affect photodetector performance, we plot in **Figure 4** (another subfigure in our database visualization dashboard) the responsivities of the same reported devices depicted in Figure 2 as a function of ligand exchange method and ligand. Not all reports provided ligand exchange methods or the choice of ligand, and these are omitted. The shape and color of the symbols indicate the chemical family of the QD material with blue stars indicating lead chalcogenides, red/orange circles indicating silver chalcogenides, and purple squares indicating mercury chalcogenides. The PbS QD-based devices tend to have the highest responsivities, irrespective of ligand chemistry and ligand exchange method, but this result can be in part attributed to the fact that these devices operate in the NIR or SWIR where higher responsivities are achievable rather than the MWIR regime. Of immediate notice in Figure 4 is that far more ligands have been explored and devices demonstrated with solid-state ligand exchange than with in-solution ligand exchange. However, despite fewer QD devices being demonstrated with in-solution ligand exchange techniques, these devices tend to have comparable or better responsivities than their solid-state ligand exchanged counterparts (for the same type of QD material). These aggregated results suggest that further development of in-solution ligand exchange techniques with other ligands may be an effective means of increasing responsivities even further. For the devices constructed from solid-state ligand exchanged QD films, we note that despite the popularity of EDT, As_2S_3 appears to generally yield higher responsivities, particularly for HgTe and HgSe. The lack of reports using As_2S_3 are most likely related to the difficulty in using these ligands, despite their promising performance thus far. The greatest variety of ligands have been used for PbS QDs, with butylamine resulting in very promising performance, particularly for in-solution based ligand exchange. Interestingly, this ligand choice hasn't been explored for QDs from the silver and mercury chalcogenide families thus far and presents as a worthwhile direction of future exploration.

Film Formation

The most common techniques for QD film formation are spin-coating, drop-casting, and dip-coating. The choice of solvent is an important factor to consider when depositing

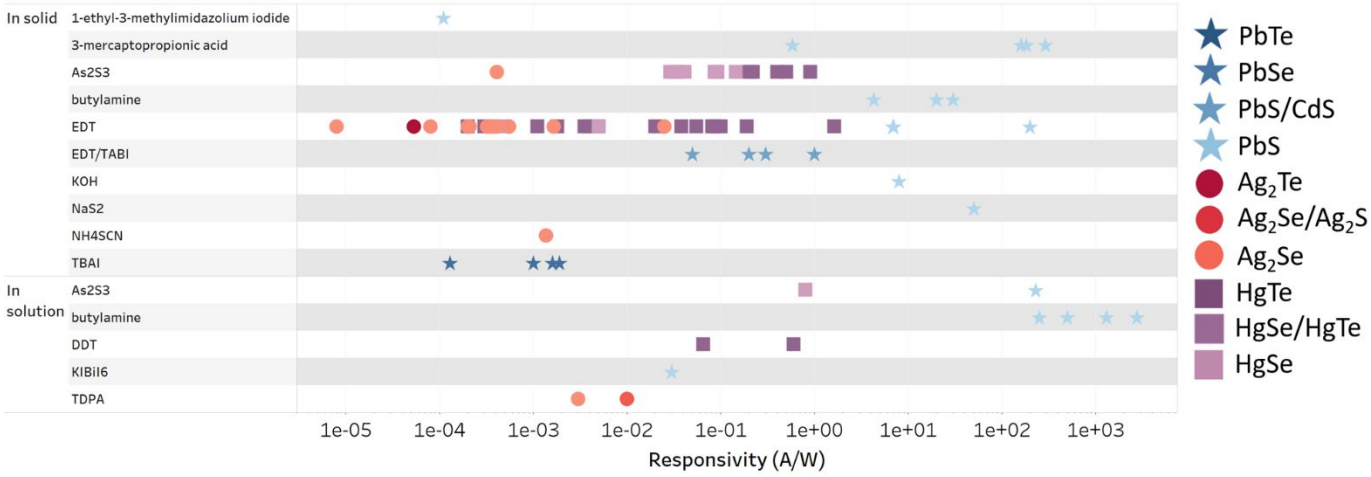

Figure 4: Responsivity of QD photodetectors as a function of ligand choice. Distinction is made between in-solution and solid-state ligand exchange methods. Shape and color correspond to different QD material.

films, as the slower rate of evaporation can typically enhance the smoothness of the film and increase the ordering of the QDs within the film. With spin-coating, a small amount of QD solution is dropped onto a substrate with the substrate then being spun at a high speed (typically 1000-5000 rpm) to uniformly distribute the solution over the substrate area. Spin-coating is the preferred method for making uniform thin films, but the significant loss of QD solution during deposition that can be quite costly if the process were to be scaled up past the research setting. Drop-casting is the simplest method where the QD solution is simply pipetted onto a substrate and dried, but problems with film uniformity can cause differing performance across the device area, making it unlikely to be viable beyond single-pixel devices. Dip-coating produces very uniform films but requires enough QD solution for the substrate to be entirely submerged and slowly removed, as the residual amount of QDs on the surface dry to form a film. Research-scale QD synthesis typically only produces amounts in the hundreds of milligrams, which means producing enough solution for dip-coating would require multiple batches or a significantly scaled-up synthesis process.

Some more advanced yet also less commonly employed methods of QD film deposition include spray-coating, ink-jet printing, slot-die coating, and electrophoretic deposition. Spray coating can be very advantageous for deposition over larger device areas,[13] with a few reports of successful devices in the MWIR[64,65] and with one such device displaying a responsivity of 0.9 A/W at 2.4 µm operating at a bias voltage of 10V, which is close to the highest responsivities reported at that wavelength for QD single pixel photodetectors (see Figure 2). Slot-die coating is the preferred deposition method for thicker films,[66] which will increase the absorption of the film, but this technique has not yet been utilized in MWIR QD detectors. Ink-jet printing of QD inks, which was popularized in the study of QD LEDs,[67] allows for precise deposition over small areas, making it an ideal possibility for deposition onto multipixel devices where uniformity over the entire device area is key.[11,68] Electrophoretic deposition is a technique in which QD film formation is driven by an applied electrical current allowing to selectively deposit onto conductive electrodes.[69] Additionally, electrophoretic deposition has the capability to form highly ordered nanocrystal films through control of the electric field, with lower electric field strength leading to slower growth and subsequently higher nanocrystal ordering.[70]

Characterization of the physical properties of MWIR QD films, such as the inter-dot spacing and QDs' degree of ordering, is a step that has been somewhat neglected and/or difficult to achieve, with only very few reports in the area.[71,72] Grazing-incidence small-angle x-ray scattering (GI-SAXS) is the predominant method that can be used to extract these key physical properties of thin QD films.[70,72,73] Ordering of QDs within a film is vital for increasing carrier mobility as well as diffusion length, which in turn will increase the efficiency of QD based devices. Likewise, decreased spacing between QDs (i.e. tighter packing) can lead to stronger coupling of the QDs, which has also been shown to improve carrier transport.[50]

Devices

Single-Pixel Devices

While the MWIR QD community's goal is to demonstrate the utility of these materials in imaging cameras, single pixel devices are more commonly employed and reported in the literature as they serve as a simple and low-cost testing platform to gain fundamental understanding as to how changes in synthesis and deposition conditions affect device performance. Additionally, fabrication of single-pixel QD devices is well established based on the decades of QD optoelectronic device research performed at shorter wavelengths, which makes interpretation of the device physics simpler. Single-pixel devices generally have either a horizontal or vertical geometry; simplified schematics of both device architectures can be seen in **Figure 5**. Devices with a horizontal geometry are either photoconductors or phototransistors. Both device types feature a channel composed of QDs between source and drain electrodes with phototransistors featuring an additional gate electrode and gate oxide to control the conductivity of the channel. The vertical geometry generally manifests itself as a photodiode that utilizes an internal electric field through a p-n, Schottky, or donor-acceptor junction.[22] Between these two geometries, the vertical device architecture is more akin to the current design of commercial multipixel focal plane arrays (FPAs) (also known as staring arrays) where the single crystalline sensing material is indium bump bonded to the ROIC (bottom contact) and a highly IR-transparent top contact or electrode is deposited on top. In practice, producing devices with a vertical architecture is more

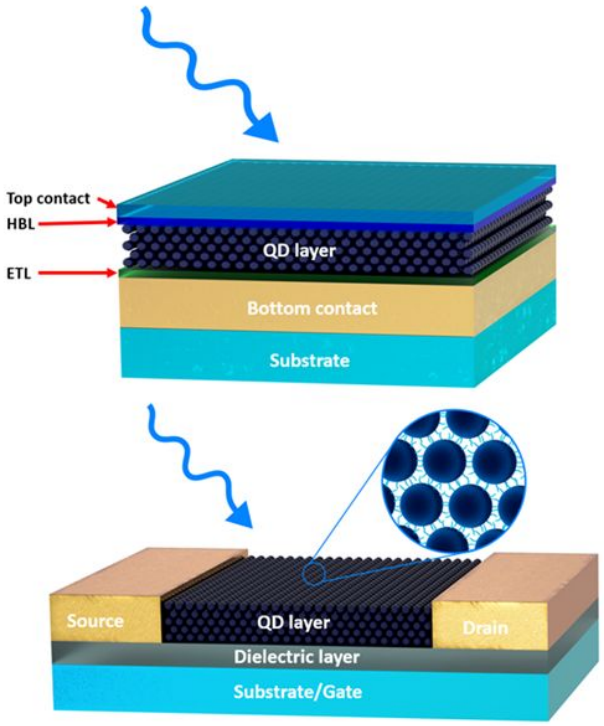

Figure 5: Schematic of simplified vertical (top) and horizontal (bottom) photodetectors. Note the top (drain) contact in the vertical devices should be IR transparent. (ETL= electron transport layer, HBL= hole blocking layer). The squiggly blue line represents incident radiation.

challenging than producing ones with a horizontal architecture since the vertically stacked devices require uniform and pinhole-free films and a highly transparent top electrode.

Vertical device architectures are advantageous for low carrier mobility materials because the distance the photogenerated carriers must traverse is set by the film thickness, which is usually on the order of hundreds of nanometers, rather than the several-micron-scale that is typical of most horizontal geometries. The vertical structure requires that at least one of the electrodes is IR-transparent, which is typically accomplished by depositing an extremely thin metal electrode (<10 nm for transparency but >5 nm for electrical continuity) or utilizing metal nanowire array electrodes.[74,75] With its high conductivity and near uniform transparency over a wide range of wavelengths, graphene is another transparent electrode candidate of increasing interest in recent years. A single layer of chemical vapor deposition (CVD) grown graphene displaying nearly 97% transparency over the MWIR range,[76–78] and it has been successfully incorporated as an electrode or transport layer in photodetectors operating in the SWIR, MWIR, and visible regimes.[79–86]

To see if any correlations exist between photodetector performance and either device geometry or film formation technique, we plot in **Figure 6** the responsivities of the same reported single-pixel photodetector devices depicted in Figure 2 as a function of device architecture (horizontal vs. vertical) and the reported film formation technique. This figure is the fourth and final subfigure in our database visualization. We note that not all publications include details on device fabrication, like the film formation method used, and these reports are not represented in the figure. Nonetheless, these aggregated results highlight how much less well-explored vertical device architectures are compared to horizontal architectures, which is likely due to the challenges described above with vertical device construction. As will be discussed in greater detail in the next section, multi-pixel IR cameras (i.e., FPAs) typically have a vertical geometry. Thus, for the current research to directly translate and help in QD camera commercialization, either vertical device geometries should be adopted in research work rather than horizontal device geometries or new conceptions of ROICs that may be amenable to lateral charge collection must be considered.

Figure 6 also makes clear how few film deposition techniques have been explored aside from spincoating and dropcasting – neither of which is particularly appealing for commercial fabrication of QD photodetectors due to the material loss and uniformity issues, respectively, that were highlighted earlier. Of the more scalable film formation methods previously discussed that include spray-coating, ink-jet printing, slot-die coating, and electrophoretic deposition, only spray-coating has been demonstrated with HgTe QDs.

We have thus far focused only on responsivity as the performance metric by which to compare single-pixel devices, in large part because this is an important and commonly reported performance metric. However, responsivity is only one of several metrics (described below) to characterize photodetector performance, and by itself, responsivity does not provide a true apples-to-apples comparison amongst devices. For one, calculations of responsivity do not account for the photodetectors' active area. Also, because radiant energy corresponding to inter- and intra-bandgap transitions is needed to generate a photocarrier, the responsivity is naturally a function of the wavelength or energy of the incident light used to perform the measurement. Responsivity can be measured using either monochromatic light (laser diode) or broadband light (black body/gas lamp) and reporting the light source and wavelength at which the responsivity measurement is performed is crucially needed to standardize results. In addition to irradiation, the bias voltage under which the device is tested affects the observed responsivity by sweeping out the photocarriers from the QD film and should always be reported with responsivity as a best practice, as well. Generally, larger biases result in larger responsivities up to a point at which all the photocarriers are swept out of the quantum dot film; once this saturation point is reached, the responsivity is no longer a function of applied bias and can be ignored as a factor in performance.

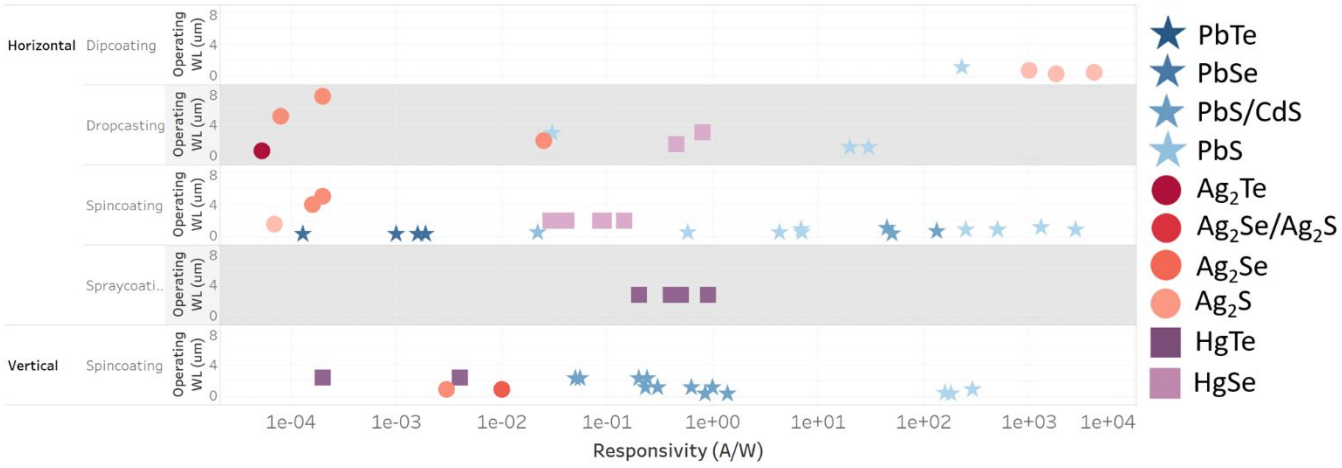

Figure 6: Responsivity off QD photodetectors as a function of deposition method and detection wavelength. Distinction is made between vertical and horizontal device architectures. Shape and color correspond to different QD material.

Specific detectivity (D*) provides another measure of a photodetector's signal-to-noise and is a better performance metric than responsivity because it accounts for the active area of the photodetector, thereby enabling absolute comparisons. Specific detectivity is directly proportional to responsivity, R, and is inversely proportional to the noise-equivalent-power (NEP), calculated as:

$$D^* = \sqrt{A\Delta f}/NEP$$

where A is the detector area. The associated units of D* are $[cm \cdot \sqrt{Hz}/W] = [Jones]$. Despite being more informative, D* is not as frequently reported as R in the literature, presumably due to the difficulty and tedious nature of accurately measuring noise. Due to the infrequent reporting and somewhat unreliable nature of D* measurements, we have chosen to primarily report R as a figure of merit in this review, but a graph of detectivity versus wavelength similar to that shown in Figure 2 can be found at:
https://public.tableau.com/authoring/IRQDphotodetectors_16384709473480/DvsWL#1.

NEP is a defined as the signal power that gives a signal-to-noise ratio of 1 and can be calculated from the total noise current (I_n)[87,88] and R, as:

$$NEP = I_n/R$$

with units of $[W/\sqrt{Hz}]$. Noise-equivalent-temperature-difference (NETD) with units of $[K/\sqrt{Hz}]$ is a similar metric to NEP that is commonly used to describe the temperature resolution of detectors and is calculated as:

$$NETD = (I_n/I_s)(T_t - T_B)$$

where I_s is the signal current, T_t is the temperature of the target, and T_B is the background temperature.

A photodetector's response time, which is generally defined as the time for the photodetector to electrically respond to the turning on or off of illumination, is also an important performance metric of photodetectors but is not always reported. The response time provides a measure of the number of trap states present and provides an upper limit for the refresh rate at which the photodetector can operate, which is of importance for commercial IR cameras. However, precisely how response times are deduced from single pixel photodetector devices is not always reported in the literature and can vary between reports. For example, one definition of the response time is the time after illumination when the responsivity reaches 0.707 of its steady-state value[89] while another definition can be correlated to rise time which is defined as the time it takes detector to go from 10% to 90% of its signal output.[90]

Another critically important yet poorly studied device performance characteristic is QD photodetectors' long-term stability and stability on exposure to oxygen and moisture. Most current QD photodetector research avoids these potential challenges by performing film fabrication and device

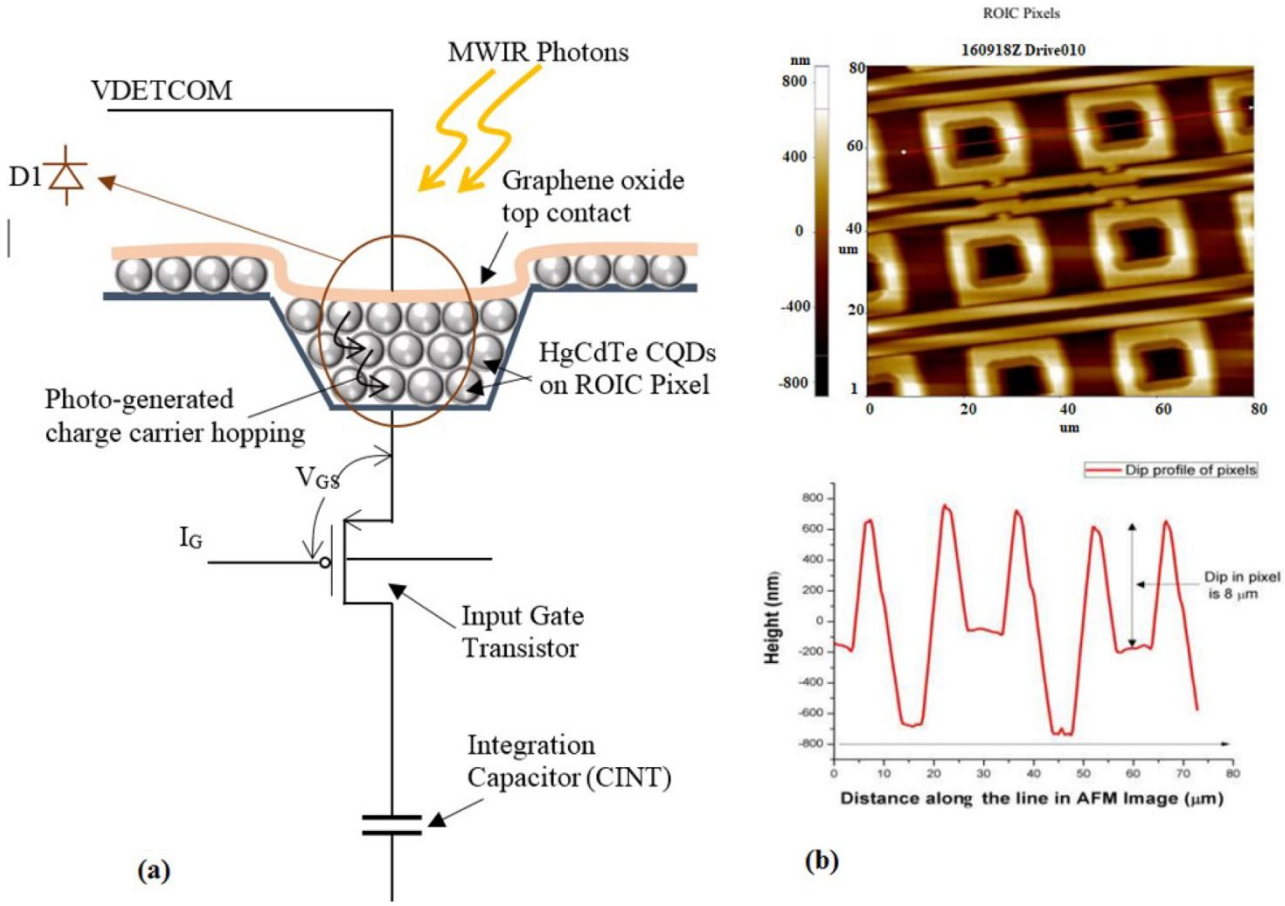

Figure 7: Schematic of an HgCdTe QD film deposited onto a ROIC, with graphene oxide top contact (left). AFM image and line scan of an uncoated ROIC (right). Reprinted from reference 81, https://creativecommons.org/licenses/by/4.0/ .

testing in oxygen-free environments and only reporting device performance immediately after device fabrication. However, performing such environmental and aging studies will be critical for commercialization of QD-based IR cameras. While Ag- and Hg-based chalcogenides are less well-characterized, lead chalcogenide QDs are known to be highly air sensitive. A couple of promising and demonstrated means of environmentally protecting QD films is through passivation with halides[31,33] or by encasing them in alumina deposited using ALD.[91] QD-based field effect transistors with an ALD-deposited alumina coating have been shown to be stable in air for at minimum several months. As an added benefit to providing environmental protection, encasing PbSe QDs with ALD-deposited alumina was also reported to increase the QD films' charge carrier mobilities; alumina-coated PbSe QD films demonstrated electron mobilities of 7 cm^2/Vs –10-100 times greater than what is typical of untreated QD films.[92]

Focal-Plane Arrays

An important leap to be made by the IR QD research community to bridge work from the research to the commercial setting is demonstration of IR imaging with QD-based devices. A few imaging demonstrations have been made where single pixel devices, like those discussed above, were rastered across a desired field of view to produce a 2D image.[37,74,83,93–95] However, such imaging demonstrations hold little practical value as rastering takes minutes to produce an image. Traditional commercial IR imagining systems quickly produce 2D images using FPAs, which consist of an IR-sensing material layered atop a ROIC, see **Figure 7**. The ROIC is a 2D pixel array that collects the photocarriers from the IR-sensing material and converts them into a signal voltage, thereby quickly producing a 2D IR image of an entire field of view without the need for rastering. To truly demonstrate their potential to compete against current commercial IR detectors, QDs must be incorporated into FPAs as the sensing material and demonstrate competitive imaging capabilities. Demonstrations of MWIR QD FPAs in the research setting seem to be hindered in large part by the high upfront costs of ROICs. ROICs are sold by only a handful of suppliers and are typically only sold as wafers consisting of ca. 100 devices, with each ROIC costing several hundred dollars; thus, R&D efforts to develop QD FPAs requires an investment of tens of thousands of dollars simply for the purchase of ROICs, which can be prohibitively high in a research setting. If this barrier can be overcome, the other barriers to producing a QD-based FPA are low: material costs of MWIR QD films are estimated to be <$5 for one FPA[96] and the cost of processing is also minimal relative to epitaxial methods. As described earlier, QD synthesis and film deposition involve commonplace organic semiconductor and wet chemistry methods, and typically only take a couple of hours to produce a functional FPA.[96]

To date, only a handful of IR imaging demonstrations of QD-based FPAs have been reported due to the immaturity of MWIR sensing QDs, high upfront cost of ROICs, and the added complexity of signals processing to generate an image from an FPA. A couple of papers have demonstrated multipixel devices similar to FPAs in the MWIR, but the pixels are isolated and the ROIC is absent, indicating that these devices cannot function as FPAs.[56,94] In the MWIR region, only four QD-based FPAs have been demonstrated. Two of these QD FPA demonstrations are by the Guyot-Sionnest Group using HgTe QDs.[96,97] In the first, HgTe QDs were drop-cast onto the ROIC and left as a monolithic film to avoid complex lithography steps. A median NETD of 102 mK and a median external quantum efficiency (EQE) of 0.64% were achieved at 100 K in the MWIR (3-5 µm) regime.[96] For context, commercial MWIR FPAs based on epitaxial InSb typically achieve an NETD < 25 mK.[98] Also for a point of comparison, single-pixel HgTe QD photoconductors have 3-4x higher EQEs in the MWIR (EQE of ~2% at 90 K and up to 2.5% at 138 K) than their multipixel FPA counterparts, demonstrating the challenge of translating performances achieved in single-pixel devices to multipixel FPAs.[99] In the second demonstration of a MWIR QD FPA by the Guyot-Sionnest group, a nearly identical FPA with a mean EQE of 0.30% and NEDT of 2.319 K was reported at 95 K using a 300 K blackbody radiation source.[97]

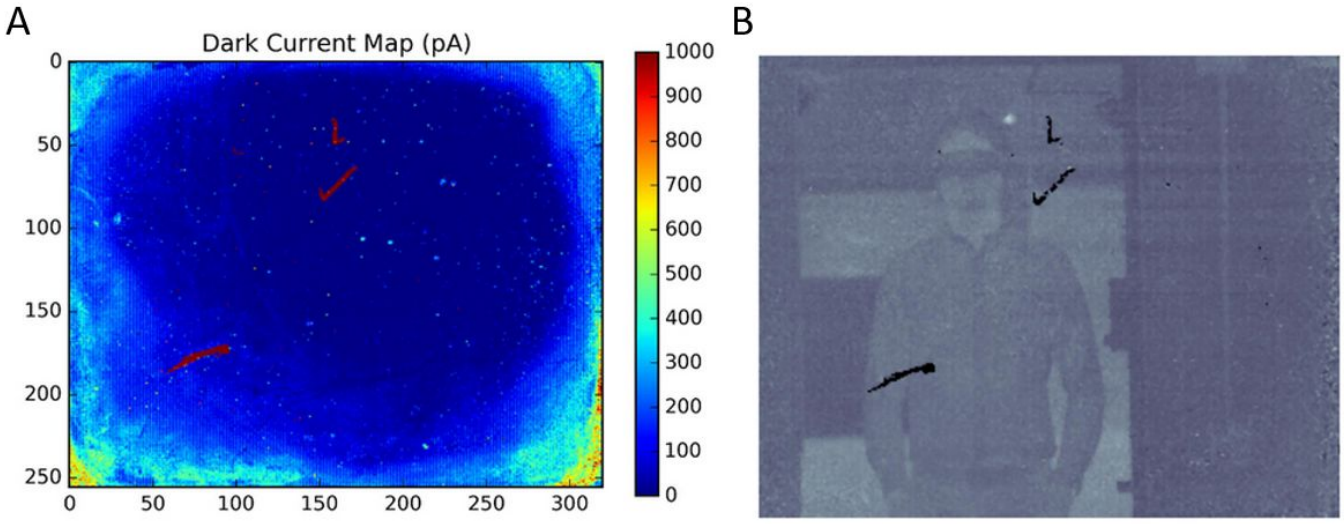

Figure 8: (A) Mapping of dark current on MWIR QD FPA and (B) image produced from the same FPA. Notice the shorted pixels resulted in dead spots on the image, reprinted/adapted with permission from reference 97.

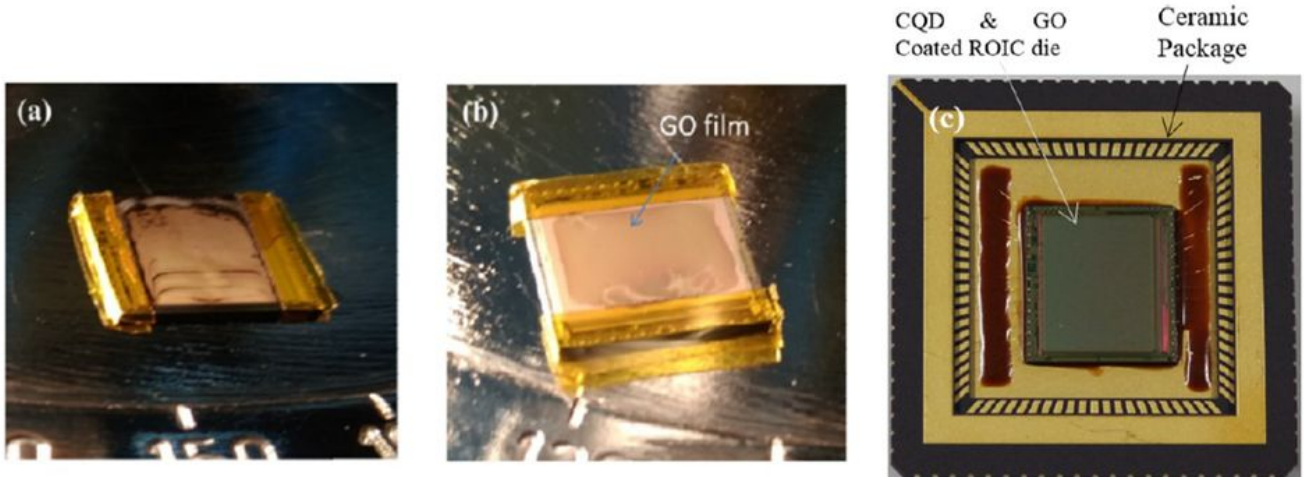

Figure 10: Photographs of ROIC die coated with HgCdTe QDs (a). Graphene oxide coated ROIC after QD deposition (b). FPA after wire bonding (c), reprinted from reference 81, https://creativecommons.org/licenses/by/4.0/ .

The HgTe QD film appears to also have been drop-cast, and the same variation in dark current/film thickness was seen. This variation is an artifact of the drop-cast drying pattern, which resulted in lower absorption and thereby lower performance in the outer pixels, along the edges of the FPA.[96] Additionally, random shorts and high conductance areas were observed, which were attributed to agglomerations in the QD film or scratches from handling of the film, see **Figure 8A**.[97] As can be seen in **Figure 8B**, these shorted pixels resulted in dead zones when producing an image. Between the two demonstrations of MWIR FPAs, the performance remained mostly the same due to common issues with QD film thickness and poor carrier transport.

In addition to HgTe QDs, FPAs have been produced with HgCdTe QDs. These QDs have a set ratio of Hg:Cd such that the composition is $Hg_{1-x}Cd_xTe$. The Rao group has demonstrated HgCdTe MWIR FPAs on a 320 x 256-pixel ROIC (FLIR ISC9705),[81,100] as seen in **Figure 9.** The QD film was deposited by spin-coating rather than drop-casting, which resulted in a more uniform film, but, like the prior QD-based FPA demonstrations, the QD film was not patterned to isolate pixels. Rather than a thin metal film, graphene oxide was used as the top contact material, which has been an effective top contact in the near-IR $Hg_{0.2}Cd_{0.8}Te$ QD devices.[101] A NEDT of 4 K at room temperature was reported in the MWIR.[81] The high NEDT is indicative of a low signal-to-noise ratio (SNR), in particular for bodies below 350 K.[102] The low SNR was attributed to non-uniformity and partial absorption of MWIR light in the graphene oxide layer.[81] This problem was remedied in a more recent paper, where the Rao group replaced the graphene oxide top contact with a very thin gold film, and deposited HgCdTe QDs onto a commercial ROIC via shock wave dispersion.[100] This deposition method resulted in improved film thickness and uniformity, verified by a 1% variation in photo response across all functioning pixels.[100] These improvements in electrode transmissivity and deposition resulted in a higher estimated EQE of 1.7% at room temperature for a 300 K black body.[100]

Further improving the performance of QD-based FPAs will require addressing several device fabrication issues, including increased film uniformity, decreased film defects, isolated individual QD pixel elements (*i.e.,* film patterning), and improved carrier transport. Film uniformity and defects are largely dictated by the film formation process. Drop-casting – the currently most-used method of film formation – tends to yield non-uniform film thicknesses due to variation in the evaporation rate of the solvent and variation in the QD concentration across the ROIC. Specifically, the drop-casting method used in HgTe QD FPAs is prone to the coffee ring effect, where a radial thickness pattern forms due to partial wetting between the substrate and QD solution, causing the edge pixels to have a thinner QD layer than in the center.[96,97] The areas with a thinner QD layer exhibit lower absorption, which reduces the signal-to-noise ratio. Patterning QD films to form isolated pixels without introducing defects to the films is another hinderance to improved QD FPA performance. The non-zero conductance of QD films, along with defects, can cause photocarriers to be collected by a neighboring pixel pad, introducing crosstalk between pixels. Crosstalk could be mitigated by patterning the monolithic QD film into pixels, thereby electrically isolating them from each other. Groups have demonstrated the ability to

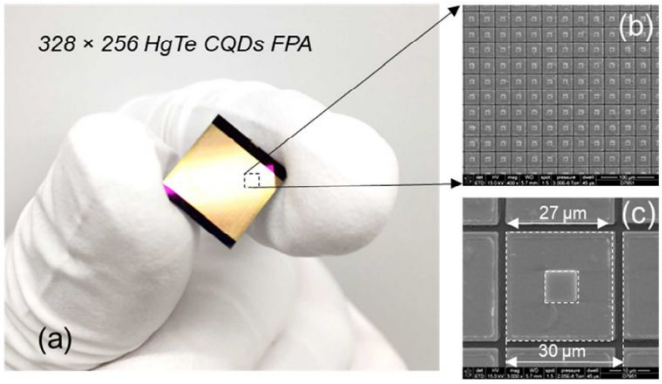

Figure 9: (a) Image of patterned HgTe QDs on a silicon substrate and (b and c) SEM images of said HgTe QD pixels, reprinted with permission from reference 94. *Copyright 2018 American Chemical Society.*

pattern QD films, but not on a ROIC. The Guyot-Sionnest group has patterned HgTe QD films with traditional photolithography and wet etch techniques,[94] and the Lhuillier group has patterned HgSe QD films with electron beam lithography and plasma etch techniques.[56] In both cases, the patterned pixels were 20-60 microns in size, as can be seen in **Figure 10,** which promisingly is of similar size to the pixels in commercial ROICs.[103] However, using these techniques to pattern QD films on ROICs may damage the underlying circuitry of the ROIC. Alignment of the ROIC pixel pads with QD pixels further complicates the patterning process. Nevertheless, producing electrically isolated pixels may reduce noise and crosstalk, improving the consistency and performance of MWIR QD FPAs. Ink-jet printing is a method that can be of great value in this endeavor,[68] however many of the reports using this method have been focused on QD LED fabrication rather than photodetection.

The performance of QD-based FPAs is also currently limited by low external quantum efficiency, which can be caused by material limitations, such as low absorption and low carrier mobility, as well as high reflectance from or absorption by the top contact. Problems with the top contact can be addressed by using an antireflective coating on top of the FPA or by using a MWIR-transparent top contact material, such as metallic nanowire arrays.[75,81] Additionally, thin QD sensing layers in MWIR FPAs result in low absorption, which limits the external quantum efficiency, but the tradeoff between layer thickness and its effect on increasing dark current must be taken into consideration.[104] An alternative approach could be the implementation of plasmonic structures, which has been shown to improve absorption of QD films by more than 30% in the NIR.[94,105–107] In addition to absorption, EQE is limited by carriers recombining before they are able to be collected, resulting in reduced photocurrent.[97] Creating thicker QD layers also increases the likelihood of recombination of photogenerated carriers. Combating carrier recombination is a two-prong approach, on one hand one would like to increase the carrier lifetime and on the other improve carrier mobility. Careful selection of capping ligands may reduce the concentration of trap states effectively increasing the carrier lifetime. Furthermore, trap states can be reduced by synthesizing core-shell quantum dots, which have shown to increase quantum efficiency by improving QD stability and resistance to oxidation and chemical degradation.[108–110] Capping ligands also have a significant effect on carrier mobility,[23] but another promising approach is addition of a 2D layer such as graphene or MoS_2, which act as a high carrier mobility transport layer, increasing the carrier mobility up into the hundreds of cm^2/Vs.[79] In hybrid 2D-QD photodetectors, the QDs act as the absorption layer, and photogenerated carriers are transferred to the 2D material where they are transported to the nearest electrode.

Conclusion and Forward Outlook

While the database serves as a useful repository for information relevant to the literature, exploring the data – generating and testing hypotheses about potential trends amongst materials, synthesis approaches, or device performances – is challenging when data is presented in such a tabular form. To address this issue, we developed an interactive visualization dashboard using Tableau that enables users to explore and interact with the data. **Figures 1, 2, 4, and 6** show screenshots from this tool, which may be accessed by anyone at:
https://public.tableau.com/app/profile/tom.nakotte/viz/IRQDphotodetectors_16384709473480/Dashboard1#1.
We chose to provide four views of the data in the dashboard to aide in answering several common questions amongst QD photodetector researchers.

While there have been many promising advances in the field of MWIR QD photodetectors, space for improvement remains in QD materials themselves, device engineering, and film deposition. In terms of material improvements, the library of capping ligands can be greatly expanded for the mercury and silver chalcogenides to assess the effects on carrier mobility, carrier lifetime, and doping. Introduction of 2D materials, which have been used quite successfully in the SWIR to increase carrier mobility, has not been thoroughly researched in the MWIR. Surface ligands have the ability to modulate energy levels as well as the Fermi level, opening up the possibility of engineering the energy levels to better align with electrodes' work functions. Ligand engineering has been successfully used to improve performance in QD solar cells, but the technique is less explored in MWIR photodetectors. Improvement of film deposition onto ROICs is a key factor in providing uniform performance throughout the device. Currently the more primitive techniques such as drop-casting and spin-coating are the most frequently used, but a more focused technique such as ink-jet printing has the potential to provide consistent coverage of all the pixels in a ROIC. As the production of ROICs becomes more commonplace it stands to reason that price would decrease, which would increase the number of devices that can be fabricated and tested. Increased production of devices is the surest way to move the field forward, as real-life testing is the most proven method. However, during the time when supply of ROICs is still limited it is important to apply educated assumptions to expand the impact and knowledge gained from each subsequent device. MWIR QD photodetectors are nearing the point where they can successfully compete with current technologies, with the possibility of providing a cheaper alternative without the need for cryogenic cooling. Improvements in carrier mobility, carrier lifetime, film deposition, and device fabrication are still needed to achieve the end goal of an uncooled affordable IR imager, however we have the tools at our disposal to make this goal a reality.

Author Contributions

S. Munyan and T. Nakotte wrote the original draft, prepared visualizations, and investigated/curated the data. A. M. Hiszpanski secured funding and wrote/edited the final draft. S. Hawks, J. Han, and S. Kang edited the final draft and validated the accuracy of the manuscript.

Conflicts of interest

There are no conflicts to declare.

Acknowledgements

This work was performed under the auspices of the U.S. Department of Energy by Lawrence Livermore National Laboratory under Contract DE-AC52-07NA27344 and supported by LDRD 19-ERD-029. This work has been reviewed for unlimited release by LLNL, IM release number LLNL-JRNL-828879.

References

1 A. P. Alivisatos, *Science (80-.).*, 1996, **271**, 933–937.
2 J. M. Pietryga, R. D. Schaller, D. Werder, M. H. Stewart, V. I. Klimov and J. A. Hollingsworth, *J. Am. Chem. Soc.*, 2004, **126**, 11752–11753.
3 G. Konstantatos and E. H. Sargent, *Infrared Phys. Technol.*, 2011, **54**, 278–282.
4 S. H. Xin, P. D. Wang, A. Yin, C. Kim, M. Dobrowolska, J. L. Merz and J. K. Furdyna, *Appl. Phys. Lett.*, 1996, **69**, 3884–3886.
5 P. B. Joyce, T. J. Krzyzewski, G. R. Bell, T. S. Jones, S. Malik, D. Childs and R. Murray, *Phys. Rev. B*, 2000, **62**, 10891–10895.
6 Y. Pu, F. Cai, D. Wang, J. X. Wang and J. F. Chen, *Ind. Eng. Chem. Res.*, 2018, 57, 1790–1802.
7 J. Jean, J. Xiao, R. Nick, N. Moody, M. Nasilowski, M. Bawendi and V. Bulović, *Energy Environ. Sci.*, 2018, **11**, 2295–2305.
8 Y. Pan, H. Bai, L. Pan, Y. Li, M. C. Tamargo, M. Sohel and J. R. Lombardi, *J. Mater. Chem.*, 2012, **22**, 23593–23601.
9 J. Zhang, R. W. Crisp, J. Gao, D. M. Kroupa, M. C. Beard and J. M. Luther, *J. Phys. Chem. Lett.*, 2015, **6**, 1830–1833.
10 J. P. Clifford, G. Konstantatos, K. W. Johnston, S. Hoogland, L. Levina and E. H. Sargent, *Nat. Nanotechnol.*, 2009, **4**, 40–44.
11 Y. Pan, L. Xue, C. Xu, T. Ding, Y. Chen and L. Li, eds. P. Zhao, Z. Ye, M. Xu, L. Yang, L. Zhang and R. Zhu, Springer Singapore, Singapore, 2021, pp. 321–328.
12 H. M. Haverinen, R. A. Myllylä and G. E. Jabbour, *Appl. Phys. Lett.*, 2009, **94**, 73108.
13 K. Song, J. Yuan, T. Shen, J. Du, J. Tian, R. Guo and T. Pullerits, *Nanomaterials*, 2019, **9**, 1–11.
14 I. J. Kramer, J. C. Minor, G. Moreno-Bautista, L. Rollny, P. Kanjanaboos, D. Kopilovic, S. M. Thon, G. H. Carey, K. W. Chou, D. Zhitomirsky, A. Amassian and E. H. Sargent, *Adv. Mater.*, 2015, **27**, 116–121.
15 M. R. Kim and D. Ma, *J. Phys. Chem. Lett.*, 2015, 6, 85–99.
16 Y. Shirasaki, G. J. Supran, M. G. Bawendi and V. Bulović, *Nat. Photonics*, 2013, 7, 13–23.
17 C. Livache, B. Martinez, N. Goubet, J. Ramade and E. Lhuillier, *Front. Chem.*, 2018, **6**, 1–11.
18 C. Gréboval, A. Chu, N. Goubet, C. Livache, S. Ithurria and E. Lhuillier, *Chem. Rev.*, 2021, **121**, 3627–3700.
19 S. E. Keuleyan, P. Guyot-Sionnest, C. Delerue and G. Allan, *ACS Nano*, 2014, **8**, 8676–8682.
20 H. S. Telescope and I. Many, .
21 R. Garwin, R. Jeanloz, J. Kimble, J. Sullivan and E. Williams, .
22 P. R. Brown, D. Kim, R. R. Lunt, N. Zhao, M. G. Bawendi, J. C. Grossman and V. Bulović, *ACS Nano*, 2014, **8**, 5863–5872.
23 Q. Lin, H. J. Yun, W. Liu, H. J. Song, N. S. Makarov, O. Isaienko, T. Nakotte, G. Chen, H. Luo, V. I. Klimov and J. M. Pietryga, *J. Am. Chem. Soc.*, 2017, **139**, 6644–6653.
24 H. Beygi, S. A. Sajjadi, A. Babakhani, J. F. Young and F. C. J. M. van Veggel, *Appl. Surf. Sci.*, 2018, **457**, 1–10.
25 K. A. Higginson, M. Kuno, J. Bonevich, S. B. Qadri, M. Yousuf and H. Mattoussi, *J. Phys. Chem. B*, 2002, **106**, 9982–9985.
26 A. Hassinen, I. Moreels, K. De Nolf, P. F. Smet, J. C. Martins and Z. Hens, *J. Am. Chem. Soc.*, 2012, **134**, 20705–20712.
27 M. Green and H. Mirzai, *J. Mater. Chem. C*, 2018, 6, 5097–5112.
28 I. A. Shuklov and V. F. Razumov, *Russ. Chem. Rev.*, 2020, **89**, 379–391.
29 Y. Pu, F. Cai, D. Wang, J. X. Wang and J. F. Chen, *Ind. Eng. Chem. Res.*, 2018, **57**, 1790–1802.
30 W. K. Koh, A. C. Bartnik, F. W. Wise and C. B. Murray, *J. Am. Chem. Soc.*, 2010, **132**, 3909–3913.
31 W. K. Bae, J. Joo, L. A. Padilha, J. Won, D. C. Lee, Q. Lin, W. K. Koh, H. Luo, V. I. Klimov and J. M. Pietryga, *J. Am. Chem. Soc.*, 2012, **134**, 20160–20168.
32 Q. Lin, N. S. Makarov, W. K. Koh, K. A. Velizhanin, C. M. Cirloganu, H. Luo, V. I. Klimov and J. M. Pietryga, *ACS Nano*, 2015, **9**, 539–547.
33 N. Killilea, M. Wu, M. Sytnyk, A. A. Yousefi Amin, O. Mashkov, E. Spiecker and W. Heiss, *Adv. Funct. Mater.*, 2019, **29**, 1807964.
34 M. Casavola, M. A. Van Huis, S. Bals, K. Lambert, Z. Hens and D. Vanmaekelbergh, *Chem. Mater.*, 2012, **24**, 294–302.
35 I. Ramiro, O. Özdemir, S. Christodoulou, S. Gupta, M. Dalmases, I. Torre and G. Konstantatos, *Nano Lett.*, 2020, **20**, 1003–1008.
36 D. Kim, D. H. Kim, J. H. Lee and J. C. Grossman, *Phys. Rev. Lett.*, 2013, **110**, 1–5.
37 A. Chu, B. Martinez, S. Ferré, V. Noguier, C. Gréboval, C. Livache, J. Qu, Y. Prado, N. Casaretto, N. Goubet, H. Cruguel, L. Dudy, M. G. Silly, G. Vincent and E. Lhuillier, *ACS Appl. Mater. Interfaces*, 2019, **11**, 33116–33123.
38 Z. Ning, O. Voznyy, J. Pan, S. Hoogland, V. Adinolfi, J. Xu, M. Li, A. R. Kirmani, J. P. Sun, J. Minor, K. W. Kemp, H. Dong, L. Rollny, A. Labelle, G. Carey, B. Sutherland, I. Hill, A. Amassian, H. Liu, J. Tang, O. M. Bakr and E. H. Sargent, *Nat. Mater.*, 2014, **13**, 822–828.
39 M. H. Zarghami, Y. Liu, M. Gibbs, E. Gebremichael, C. Webster and M. Law, *ACS Nano*, 2010, **4**, 2475–2485.
40 S. Keuleyan, E. Lhuillier, V. Brajuskovic and P. Guyot-Sionnest, *Nat. Photonics*, 2011, **5**, 489–493.
41 Z. Deng, K. S. Jeong and P. Guyot-Sionnest, *ACS Nano*,

2014, **8**, 11707–11714.

42 C. Livache, B. Martinez, A. Robin, N. Goubet, B. Dubertret, H. Wang, S. Ithurria, H. Aubin and E. Lhuillier, *Phys. status solidi*, 2018, **215**, 1700294.

43 A. Robin, C. Livache, S. Ithurria, E. Lacaze, B. Dubertret and E. Lhuillier, *ACS Appl. Mater. Interfaces*, 2016, **8**, 27122–27128.

44 S. Bin Hafiz, M. M. Al Mahfuz, M. R. Scimeca, S. Lee, S. J. Oh, A. Sahu and D. K. Ko, *Phys. E Low-Dimensional Syst. Nanostructures*, , DOI:10.1016/j.physe.2020.114223.

45 B. Martinez, C. Livache, L. D. Notemgnou Mouafo, N. Goubet, S. Keuleyan, H. Cruguel, S. Ithurria, H. Aubin, A. Ouerghi, B. Doudin, E. Lacaze, B. Dubertret, M. G. Silly, R. P. S. M. Lobo, J.-F. Dayen and E. Lhuillier, *ACS Appl. Mater. Interfaces*, 2017, **9**, 36173–36180.

46 W. H. Strehlow and E. L. Cook, *J. Phys. Chem. Ref. Data*, 1973, **2**, 163–200.

47 C.-N. Zhu, P. Jiang, Z.-L. Zhang, D.-L. Zhu, Z.-Q. Tian and D.-W. Pang, *ACS Appl. Mater. Interfaces*, 2013, **5**, 1186–1189.

48 M. Park, D. Choi, Y. Choi, H. B. Shin and K. S. Jeong, *ACS Photonics*, 2018, **5**, 1907–1911.

49 A. Sahu, A. Khare, D. D. Deng and D. J. Norris, *Chem. Commun.*, 2012, **48**, 5458–5460.

50 C. R. Kagan and C. B. Murray, *Nat. Nanotechnol.*, 2015, **10**, 1013–1026.

51 S. Bin Hafiz, M. M. Al Mahfuz and D.-K. Ko, *ECS Trans.*, 2020, **97**, 109–115.

52 M. R. Scimeca, N. Mattu, I. J. Paredes, M. N. Tran, S. J. Paul, E. S. Aydil and A. Sahu, *J. Phys. Chem. C*, 2021, **125**, 17556–17564.

53 B. Martinez, C. Livache, N. Goubet, A. Jagtap, H. Cruguel, A. Ouerghi, E. Lacaze, M. G. Silly and E. Lhuillier, *J. Phys. Chem. C*, 2018, **122**, 859–865.

54 M. R. Kim and D. Ma, *J. Phys. Chem. Lett.*, 2015, **6**, 85–99.

55 R. Wang, Y. Shang, P. Kanjanaboos, W. Zhou, Z. Ning and E. H. Sargent, *Energy Environ. Sci.*, 2016, **9**, 1130–1143.

56 E. Lhuillier, M. Scarafagio, P. Hease, B. Nadal, H. Aubin, X. Z. Xu, N. Lequeux, G. Patriarche, S. Ithurria and B. Dubertret, *Nano Lett.*, 2016, **16**, 1282–1286.

57 B. Martinez, J. Ramade, C. Livache, N. Goubet, A. Chu, C. Gréboval, J. Qu, W. L. Watkins, L. Becerra, E. Dandeu, J. L. Fave, C. Méthivier, E. Lacaze and E. Lhuillier, *Adv. Opt. Mater.*, 2019, **7**, 1900348.

58 X. Lan, M. Chen, M. H. Hudson, V. Kamysbayev, Y. Wang, P. Guyot-Sionnest and D. V Talapin, *Nat. Mater.*, 2020, **19**, 323–329.

59 M. Chen, X. Lan, X. Tang, Y. Wang, M. H. Hudson, D. V Talapin and P. Guyot-Sionnest, *ACS Photonics*, 2019, **6**, 2358–2365.

60 M. Chen, H. Yu, S. V. Kershaw, H. Xu, S. Gupta, F. Hetsch, A. L. Rogach and N. Zhao, *Adv. Funct. Mater.*, 2014, **24**, 53–59.

61 J. Gao, S. Jeong, F. Lin, P. T. Erslev, O. E. Semonin, J. M. Luther and M. C. Beard, *Appl. Phys. Lett.*, 2013, **102**, 43506.

62 S. J. Baik, K. Kim, K. S. Lim, S. Jung, Y.-C. Park, D. G. Han, S. Lim, S. Yoo and S. Jeong, *J. Phys. Chem. C*, 2011, **115**, 607–612.

63 M. Law, J. M. Luther, Q. Song, B. K. Hughes, C. L. Perkins and A. J. Nozik, *J. Am. Chem. Soc.*, 2008, **130**, 5974–5985.

64 M. Chen, H. Lu, N. M. Abdelazim, Y. Zhu, Z. Wang, W. Ren, S. V Kershaw, A. L. Rogach and N. Zhao, *ACS Nano*, 2017, **11**, 5614–5622.

65 M. E. Cryer and J. E. Halpert, *ACS Photonics*, 2018, **5**, 3009–3015.

66 J. Z. Fan, M. Vafaie, K. Bertens, M. Sytnyk, J. M. Pina, L. K. Sagar, O. Ouellette, A. H. Proppe, A. S. Rasouli, Y. Gao, S. W. Baek, B. Chen, F. Laquai, S. Hoogland, F. P. G. De Arquer, W. Heiss and E. H. Sargent, *Nano Lett.*, 2020, **20**, 5284–5291.

67 C. Xiang, L. Wu, Z. Lu, M. Li, Y. Wen, Y. Yang, W. Liu, T. Zhang, W. Cao, S.-W. Tsang, B. Shan, X. Yan and L. Qian, *Nat. Commun.*, 2020, **11**, 1646.

68 M. Böberl, M. V. Kovalenko, S. Gamerith, E. J. W. List and W. Heiss, *Adv. Mater.*, 2007, **19**, 3574–3578.

69 J. Zhao, L. Chen, D. Li, Z. Shi, P. Liu, Z. Yao, H. Yang, T. Zou, B. Zhao, X. Zhang, H. Zhou, Y. Yang, W. Cao, X. Yan, S. Zhang and X. W. Sun, *Nat. Commun.*, 2021, **12**, 4603.

70 Y. Yu, D. Yu and C. A. Orme, *Nano Lett.*, 2017, **17**, 3862–3869.

71 D. D. W. Grinolds, P. R. Brown, D. K. Harris, V. Bulovic and M. G. Bawendi, *Nano Lett.*, 2015, **15**, 21–26.

72 M. Buljan, N. Radić, S. Bernstorff, G. Dražić, I. Bogdanović-Radović and V. Holý, *Acta Crystallogr. Sect. A*, 2012, **68**, 124–138.

73 L. Sun, J. J. Choi, D. Stachnik, A. C. Bartnik, B.-R. Hyun, G. G. Malliaras, T. Hanrath and F. W. Wise, *Nat. Nanotechnol.*, 2012, **7**, 369–373.

74 X. Tang, M. M. Ackerman, M. Chen and P. Guyot-Sionnest, *Nat. Photonics*, 2019, **13**, 277–282.

75 S. Bin Hafiz, M. M. Al Mahfuz and D.-K. Ko, *ACS Appl. Mater. Interfaces*, 2021, **13**, 937–943.

76 C.-C. Lin, D.-Y. Wang, K.-H. Tu, Y.-T. Jiang, M.-H. Hsieh, C.-C. Chen and C.-W. Chen, *Appl. Phys. Lett.*, 2011, **98**, 263509.

77 C. Lee, J. Y. Kim, S. Bae, K. S. Kim, B. H. Hong and E. J. Choi, *Appl. Phys. Lett.*, 2011, **98**, 71905.

78 F. G. Micallef, P. K. Shrestha, D. Chu, K. McEwan, G. Rughoobur, T. Carey, N. Coburn, F. Torrisi, O. Txoperena and A. Zurutuza, *Thin Solid Films*, 2018, **660**, 411–420.

79 T. Nakotte, H. Luo and J. Pietryga, *Nanomaterials*, , DOI:10.3390/nano10010172.

80 Y. Che, Y. Zhang, X. Cao, H. Zhang, X. Song, M. Cao, Y. Yu, H. Dai, J. Yang, G. Zhang and J. Yao, *ACS Appl. Mater. Interfaces*, 2017, **9**, 32001–32007.

81 A. Chatterjee, N. B. Pendyala, A. Jagtap and K. S. R. Koteswara Rao, *e-Journal Surf. Sci. Nanotechnol.*, 2019, **17**, 95–100.

82 G. Konstantatos, M. Badioli, L. Gaudreau, J. Osmond, M. Bernechea, F. P. G. de Arquer, F. Gatti and F. H. L. Koppens, *Nat. Nanotechnol.*, 2012, **7**, 363–368.

83 S. Goossens, G. Navickaite, C. Monasterio, S. Gupta, J. J. Piqueras, R. Pérez, G. Burwell, I. Nikitskiy, T. Lasanta, T. Galán, E. Puma, A. Centeno, A. Pesquera, A. Zurutuza, G. Konstantatos and F. Koppens, *Nat. Photonics*, 2017, **11**, 366–371.

84 X. Tang, M. Chen, A. Kamath, M. M. Ackerman and P. Guyot-Sionnest, *ACS Photonics*, 2020, **7**, 1117–1121.
85 U. N. Noumbé, C. Gréboval, C. Livache, A. Chu, H. Majjad, L. E. Parra López, L. D. N. Mouafo, B. Doudin, S. Berciaud, J. Chaste, A. Ouerghi, E. Lhuillier and J.-F. Dayen, *ACS Nano*, 2020, **14**, 4567–4576.
86 C. Gréboval, U. N. Noumbé, A. Chu, Y. Prado, A. Khalili, C. Dabard, T. H. Dang, S. Colis, J. Chaste, A. Ouerghi, J.-F. Dayen and E. Lhuillier, *Appl. Phys. Lett.*, 2020, **117**, 251104.
87 A. De Iacovo, C. Venettacci, L. Colace, L. Scopa and S. Foglia, *Appl. Phys. Lett.*, 2017, **111**, 211104.
88 R. Saran and R. J. Curry, *Nat. Photonics*, 2016, 10, 81–92.
89 P. G. Datskos and N. V. Lavrik, *Oak Ridge Natl. Lab.*, 2014, 145–188.
90 Richard S. Quimby, in *Photonics and Lasers*, John Wiley & Sons, Inc., 2006.
91 Y. Liu, M. Gibbs, C. L. Perkins, J. Tolentino, M. H. Zarghami, J. Bustamante and M. Law, *Nano Lett.*, 2011, **11**, 5349–5355.
92 Y. Liu, J. Tolentino, M. Gibbs, R. Ihly, C. L. Perkins, Y. Liu, N. Crawford, J. C. Hemminger and M. Law, *Nano Lett.*, 2013, **13**, 1578–1587.
93 X. Tang, M. M. Ackerman, G. Shen and P. Guyot-Sionnest, *Small*, 2019, **15**, 1804920.
94 X. Tang, M. M. Ackerman and P. Guyot-Sionnest, *ACS Nano*, 2018, **12**, 7362–7370.
95 T. Rauch, M. Böberl, S. F. Tedde, J. Fürst, M. V Kovalenko, G. Hesser, U. Lemmer, W. Heiss and O. Hayden, *Nat. Photonics*, 2009, **3**, 332–336.
96 C. Buurma, R. E. Pimpinella, A. J. Ciani, J. S. Feldman, C. H. Grein and P. Guyot-Sionnest, *Opt. Sensing, Imaging, Phot. Count. Nanostructured Devices Appl. 2016*, 2016, **9933**, 993303.
97 A. J. Ciani, R. E. Pimpinella, C. H. Grein and P. Guyot-Sionnest, in *Infrared Technology and Applications XLII*, eds. B. F. Andresen, G. F. Fulop, C. M. Hanson, J. L. Miller and P. R. Norton, SPIE, 2016, vol. 9819, p. 981919.
98 Neutrino Midwave Infrared Cooled Camera Module | FLIR Systems.
99 P. Guyot-Sionnest and J. A. Roberts, *Appl. Phys. Lett.*, 2015, **107**, 253104.
100 A. Chatterjee, J. Balakrishnan, N. B. Pendyala and K. S. R. Koteswara Rao, *Appl. Surf. Sci. Adv.*, 2020, **1**, 100024.
101 A. M. Jagtap, V. Varade, B. Konkena, K. P. Ramesh, A. Chatterjee, A. Banerjee, N. B. Pendyala and K. S. R. Koteswara Rao, *J. Appl. Phys.*, , DOI:10.1063/1.4942018.
102 A. Chatterjee, N. Babu and K. S. R. K. Rao, in *INTERNATIONAL CONFERENCE ON EMERGING APPLICATIONS IN MATERIAL SCIENCE AND TECHNOLOGY: ICEAMST 2020*, AIP Publishing, 2020, vol. 2235, p. 020033.
103 B. Lutterbeck and Z. Schluss, 2007, 1–9.
104 J. Z. Fan, M. Vafaie, K. Bertens, M. Sytnyk, J. M. Pina, L. K. Sagar, O. Ouellette, A. H. Proppe, A. S. Rasouli, Y. Gao, S. W. Baek, B. Chen, F. Laquai, S. Hoogland, F. P. G. De Arquer, W. Heiss and E. H. Sargent, *Nano Lett.*, 2020, **20**, 5284–5291.
105 M. Chen, L. Shao, S. V. Kershaw, H. Yu, J. Wang, A. L. Rogach and N. Zhao, *ACS Nano*, 2014, **8**, 8208–8216.
106 S. L. Diedenhofen, D. Kufer, T. Lasanta and G. Konstantatos, *Light Sci. Appl.*, 2015, **4**, e234.
107 X. Tang, G. fu Wu and K. W. C. Lai, *J. Mater. Chem. C*, 2017, **5**, 362–369.
108 M. A. Hines and P. Guyot-Sionnest, *J. Phys. Chem.*, 1996, **100**, 468–471.
109 X. Peng, M. C. Schlamp, A. V. Kadavanich and A. P. Alivisatos, *J. Am. Chem. Soc.*, 1997, **119**, 7019–7029.
110 H. Y. Xie, J. G. Liang, Y. Liu, Z. L. Zhang, D. W. Pang, Z. K. He, Z. X. Lu and W. H. Huang, *J. Nanosci. Nanotechnol.*, 2005, **5**, 880–886.